

Relationship between A-site Cation and Magnetic Structure in 3d-5d-4f Double Perovskite Iridates Ln_2NiIrO_6 ($Ln=La, Pr, Nd$)

T. Ferreira,^{1,2} S. Calder,^{3,*} D. S. Parker,¹ M. H. Upton,⁴ A. S. Sefat,¹ and H.-C. zur Loye^{2,†}

¹*Materials Science and Technology Division, Oak Ridge National Laboratory, Oak Ridge, TN 37831.*

²*Department of Chemistry and Biochemistry, University of South Carolina, Columbia, SC 2920.*

³*Neutron Scattering Division, Oak Ridge National Laboratory, Oak Ridge, Tennessee 37831, USA.*

⁴*Advanced Photon Source, Argonne National Laboratory, Argonne, Illinois 60439, USA.*

We report a comprehensive investigation of Ln_2NiIrO_6 ($Ln = La, Pr, Nd$) using thermodynamic and transport properties, neutron powder diffraction, resonant inelastic x-ray scattering, and density functional theory (DFT) calculations to investigate the role of A-site cations on the magnetic interactions in this family of hybrid 3d-5d-4f compositions. Magnetic structure determination using neutron diffraction reveals antiferromagnetism for La_2NiIrO_6 , a collinear ferrimagnetic Ni/Ir state that is driven to long range antiferromagnetism upon the onset of Nd ordering in Nd_2NiIrO_6 , and a non-collinear ferrimagnetic Ni/Ir sublattice interpenetrated by a ferromagnetic Pr lattice for Pr_2NiIrO_6 . For Pr_2NiIrO_6 heat capacity results reveal the presence of two independent magnetic sublattices and transport resistivity indicates insulating behavior and a conduction pathway that is thermally mediated. First principles DFT calculation elucidates the existence of the two independent magnetic sublattices within Pr_2NiIrO_6 and offers insight into the behavior in La_2NiIrO_6 and Nd_2NiIrO_6 . Resonant inelastic x-ray scattering is consistent with spin-orbit coupling splitting the t_{2g} manifold of octahedral Ir^{4+} into a $J_{eff} = \frac{1}{2}$ and $J_{eff} = \frac{3}{2}$ state for all members of the series considered.

I. INTRODUCTION

Perovskites are one of the most studied solid-state materials due to their modular structure allowing for the incorporation of a wide range of elements, within the limitations outlined by the Goldschmidt tolerance factor [1–4]. The ability to stabilize a wide variety of elements with different, and often competing, physical properties within the same material makes the perovskite structure a model system to study a rich diversity of magnetic and electronic properties [5–24]. Hybrid 3d-5d(4d) based materials that adopt the perovskite structure type host an array of physical properties originating from a delicate balance of interactions. For example, unpaired 3d electrons strongly correlate to 2p oxygen electrons in a perovskite lattice, often resulting in technologically useful properties such as ferromagnetism [25], ferroelectricity [26], and multiferroicism [5]. By contrast, the greater orbital extent of heavier 5d elements, weaker electron correlation strength, and stronger spin-orbit coupling (SOC) can lead to metal-insulator transitions [27], topological insulators [28], superconductivity [29] and a split of the t_{2g} manifold into a $J_{eff} = \frac{1}{2}$ and $J_{eff} = \frac{3}{2}$ state, as observed in Sr_2IrO_4 [30], that can lead to new routes to Mott and other exotic insulating states [30–41]. Hybrid perovskites containing both 3d and 5d elements have been reported to exhibit a wide range of properties characteristic of both 3d and 5d containing oxides, in addition to extremely high magnetic ordering temperatures, (Curie temperature of $T_c = 725$ K) such as that observed in Sr_2CrOsO_6 , further motivating the study of perovskites as a host lattice to investigate the balance of competing interactions.

Compared to the single perovskite (ABO_3) system with only one B site, the double perovskite ($A_2BB'O_6$) allows

for two crystallographically unique sites on which up to three magnetic ions may reside. Most studies of double perovskites limit the number of magnetic cations to one or two, often on the B and B' site for ease of study, although exceptions do exist [8, 13]. This allows for the possibility of studying the interaction between superexchange (B-O-B') and super-superexchange interactions (B-O-B'-O-B), such as that studied in Ca_2MOsO_6 ($M = Co, Ni$) [14, 17]. There it was demonstrated that strong antiferromagnetic coupling between Os and Co/Ni stabilize the ferrimagnetic ground state, indicating strong superexchange interactions, and weak super-superexchange interactions. Interestingly, the chemical substitution of nonmagnetic Ca in these materials for Sr results in Sr_2CoOsO_6 , which has been shown to exhibit strong super-superexchange interactions (Os-O-Co-O-Os and Co-O-Os-O-Os) resulting in two interpenetrating antiferromagnetic magnetic sublattices [15]. These sublattices have independent magnetic ordering temperatures (Os: $T_N = 108$ K; Co: $T_N = 70$ K) and distinct magnetic propagation vectors (Os: $k=(\frac{1}{2}, \frac{1}{2}, 0)$; Co: $k=(\frac{1}{2}, 0, \frac{1}{2})$) [15], in direct contrast to the nearly isostructural and isovalent Ca_2CoOsO_6 analog. The subtle structural change associated with substitution of Ca for Sr resulted in a drastic change in superexchange strength, magnetic ordering temperature, and the nature of the long range magnetic order (ferrimagnetic Ca_2CoOsO_6 and antiferromagnetic Sr_2CoOsO_6), exemplifying how sensitive these hybrid perovskites are to chemical changes [42].

The Kanamori-Goodenough rules [43] have provided a set of semi-empirical guidelines to understand the complex relationship between superexchange interactions and magnetic order in condensed matter systems. These rules provide a method for determining the sign of superexchange interactions, predicting antiferromagnetic order for linear M-X-M interactions (where X is a bridging anionic unit such as a chalcogenide or halide) and ferromagnetic order for 90° M-X-M interactions. Although these rules have been shown

* caldersa@ornl.gov

† zurloye@mailbox.sc.edu

to successfully predict superexchange interactions for perovskites, poor energetic overlap between magnetic cations, such as those in mixed $3d$ - $5d$ oxides, can lead to violations of these rules. One such example is the hybrid $3d$ - $5d$ double perovskite $\text{Sr}_2\text{FeOsO}_6$, [44, 45] in which the bent Os-O-Fe superexchange interaction in the ab -plane exhibited antiferromagnetic order, and these bonds exhibited ferromagnetism in the c -axis despite the 180° Os-O-Fe bond angle. Exceptions such as these continue to motivate the detailed study of hybrid $3d$ - $5d$ complex oxides, and serve as a motivating factor for this work, which extends to the rarely studied $3d$ - $5d$ - $4f$ compositions.

Here we report a comprehensive investigation of $\text{Ln}_2\text{NiIrO}_6$ ($\text{Ln} = \text{La}, \text{Pr}, \text{Nd}$). We begin with measurements of all compounds with neutron powder diffraction and resonant inelastic x-ray scattering (RIXS) to determine the magnetic structure and explore how SOC affects the t_{2g} manifold of the Ir ion. The remainder of the manuscript focuses on $\text{Pr}_2\text{NiIrO}_6$ using thermodynamic, transport property and density functional theory (DFT) calculations. The results allow insights into the role superexchange plays in these scarcely studied hybrid $3d$ - $5d$ - $4f$ compositions with variable A site cations. These materials were previously reported by some of the authors of this manuscript [8] and this study seeks to elucidate the magnetic structure of all three compositions. Several magnetic ordered phases are observed as the different magnetic ions order. The presence of independent magnetic sublattices in $\text{Pr}_2\text{NiIrO}_6$ is explored in detail. This approach allows us to go beyond the Kanamori-Goodenough rules to determine the varied magnetic interactions and ground states in these related materials as the rare earth ion is altered and the temperature is tuned.

II. EXPERIMENTAL DETAILS

A. Sample synthesis

Ln_2O_3 (Alfa Aesar 99.99%) and Pr_6O_{11} (Alfa Aesar 99.9%) were all heated in air at 1000°C in a tube furnace overnight to remove any possible hydroxide or carbonate impurities. Pr_6O_{11} (Alfa Aesar, 99.99%) was reduced to Pr_2O_3 under 5% hydrogen at 1000°C in a tube furnace overnight. NiO (Sigma Aldrich, 99.999%) and Ir powder (Engelhard, 99.9995%) were used as received. Polycrystalline samples of $\text{Ln}_2\text{NiIrO}_6$ were prepared by intimately grinding Ln_2O_3 , Ni, and Ir metal in stoichiometric amounts and heating the resultant powder in air in an alumina crucible with a loose fitting lid. The samples were heated to 800°C for 72 hours, 900°C for 72 hours, and then 975°C for 168 hours with intermediate grindings in a programmable furnace. For $\text{Pr}_2\text{NiIrO}_6$, an additional heating at 1025°C for 96 hours with intermediate grindings was necessary.

B. Physical property measurements

Temperature dependent heat capacity was measured using a Quantum Design physical property measurement system (PPMS) on polycrystalline powder of $\text{Pr}_2\text{NiIrO}_6$ that were pressed into a pellet and sintered at 400°C for 72 hours. The electrical resistance of pressed and sintered pellets cut into a rectangular shape was recorded as a function of temperature by the four-probe method. Silver paint electrodes using platinum wires were used as contact points. The temperature was controlled from 380 K down to 1.8 K using a Quantum Design PPMS.

C. Neutron powder diffraction

Neutron diffraction measurements were performed on 5 gram samples of $\text{Ln}_2\text{NiIrO}_6$ at Oak Ridge National Laboratory on the HB-2A Powder diffraction instrument at the High Flux Isotope Reactor (HFIR) [46, 47]. Measurements were performed with the samples loaded into 1 mm Al annular cans to reduce neutron absorption from the Ir ion. The outer diameter of the sample cans were 15 mm. A wavelength of 2.41 \AA was selected with a vertically focusing germanium monochromator on the Ge(113) reflection. Data were collected over a 2θ angular range of $5^\circ - 130^\circ$ in steps of 0.05° . The detector efficiency was normalized with a vanadium measurement. The $\text{La}_2\text{NiIrO}_6$ and $\text{Nd}_2\text{NiIrO}_6$ samples were cooled in a top-loading closed cycle refrigerator (CCR) to reach 4 K and a ^4He cryostat was used for $\text{Pr}_2\text{NiIrO}_6$ to get to the lower temperature of 1.5 K. FullProf was utilized for the Rietveld refinement and determination of the propagation vectors (k vectors) [48]. The magnetic space groups were determined using the Bilbao Crystallographic Server [49, 50]. Representational analysis was also used during the magnetic structure determination process with SARAh [51]. See Supplemental Material at [52] for the mcif files of the determined magnetic structures.

D. Resonant Inelastic X-ray Scattering

RIXS was carried out on the MERIX spectrometer, sector-27 at the Advanced Photon Source (APS) [53]. The incident energy was tuned to the Ir L_3 -edge (11.215 keV) resonant edge to enhance the Ir scattering. The inelastic energy was measured with the use of a Si(844) analyzer. The energy resolution was determined to be 35 meV at full width half maximum (FWHM), based on fitting the quasi-elastic line to a charge peak. The scattering plane and incident photon polarization were both horizontal, i.e. π incident polarization, with the incident beam focused to a size of $40 \times 25 \mu\text{m}^2$ ($H \times V$) at the sample position. To minimize elastic scattering measurements were performed with 2θ at 90° in horizontal geometry. All measurements were performed on powder samples mounted onto an Al block sealed with Kapton paper with space for all three samples in a custom mount. The temperature was controlled with a CCR and measurements taken at 5

K, 30 K and 150 K to cover the different regions of magnetic ordering in the materials.

E. First Principles Calculations

First principles calculations were performed using the all-electron linearized augmented planewave (LAPW) DFT code WIEN2K [54], within the generalized gradient approximation of Perdew, Burke and Ernzerhof [55]. LAPW sphere radii of 1.62, 1.98, 1.98 and 2.35 Bohr were used respectively for Oxygen, Nickel, Iridium and Praseodymium, respectively, with an RK_{max} value of 8.0 employed. Here RK_{max} is the product of the smallest sphere radius (in this case Oxygen) and the largest plane-wave expansion wavevector. All calculations used an optimized structure, with the lattice constants and space group taken from the experimental measurement and all internal coordinates not dictated by symmetry relaxed within a ferromagnetic Pr-Ni configuration (note that in this case Ir carries a small negative moment). Sufficient numbers of k-points (generally between 200 and 600 in the full Brillouin zone) to describe the magnetic order were used for all calculations. For the detailed magnetic calculations (not the optimization), a U value of 5 eV was applied to the Pr 4f orbitals. This value corresponds with that chosen in recent work on Pr-containing transition metal, perovskite oxides [56]. We also include straight GGA results as this provides insight regarding the effect of the Hubbard U on the exchange energetics.

III. RESULTS AND DISCUSSION

A. Magnetic Structure Determination

Neutron powder diffraction measurements were performed on all $Ln_2\text{NiIrO}_6$ materials to determine the magnetic structure in different temperature regimes. The crystal structures were previously determined with single crystal x-ray diffraction to be $P2_1/n$ (#14) [8].

1. $\text{La}_2\text{NiIrO}_6$

	x	y	z	Site
La	0.008(1)	0.546(5)	0.753(2)	4e
Ir	0	0	0	2a
Ni	0	0	0.5	2b
O1	0.084(1)	0.019(8)	0.260(2)	4e
O2	0.211(4)	0.280(2)	-0.047(1)	4e
O3	0.207(4)	0.305(2)	0.540(2)	4e

TABLE I. Crystal structure of $\text{La}_2\text{NiIrO}_6$ at 100 K from neutron refinement in the $P2_1/n$ space group with $a=5.566(2)\text{\AA}$, $b=5.630(2)\text{\AA}$, $c=7.888(3)\text{\AA}$, $\beta=90.09(2)^\circ$.

We first begin with the magnetic structure determination of $\text{La}_2\text{NiIrO}_6$, that is expected to only contain 3d (Ni^{2+}) and

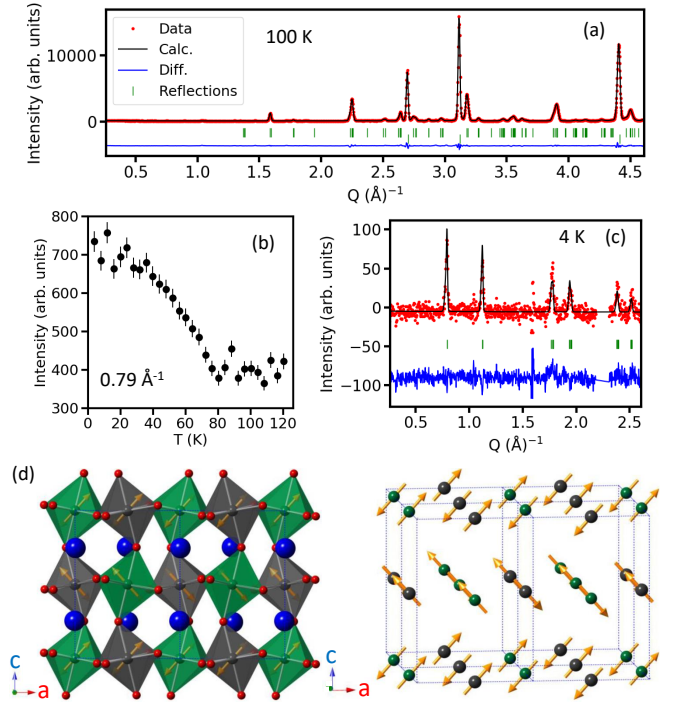


FIG. 1. Magnetic structure of $\text{La}_2\text{NiIrO}_6$. (a) Refinement of neutron powder diffraction data at 100 K to the $P2_1/n$ crystal structure (upper tick marks). Lower Tick marks correspond to the Al scattering from the sample holder. (b) Intensity of the reflection at 0.79\AA^{-1} as a function of temperature. (c) Magnetic structure model fit to the intensity obtained by subtracting the 100 K neutron diffraction data from the 4 K measurement. (d) Polyhedral representation of the magnetic and nuclear structure of $\text{La}_2\text{NiIrO}_6$ and magnetic-atom only representation with La (blue), Ni (green), Ir (grey) and O (red) atoms shown. The non-magnetic unit cell is outlined with the blue dashed line. The magnetic unit cell is doubled along the a and b -axis.

5d (Ir^{4+}) magnetic ion ordering and a non-magnetic 4f ion (La^{3+}). $\text{La}_2\text{NiIrO}_6$ was reported to undergo an antiferromagnetic transition around 75 K, with indications of further magnetic anomalies within this phase [8]. A powder sample of $\text{La}_2\text{NiIrO}_6$ was measured at four different temperatures: 4 K, 40 K, 65 K, and 100 K. This allowed the anomalies in the reported SQUID measurements [8] to be explored and disentangle the evolution of any magnetic ordering. The 100 K measurement is above the highest observed magnetic transition and was used to obtain a structural model in the paramagnetic phase based on the previously reported structure of $P2_1/n$, shown in Fig. 1(a) and Table I. No impurities were detected in the neutron data. Upon cooling below 80 K, the temperature regime in which magnetic order is expected for $\text{La}_2\text{NiIrO}_6$, the presence of additional intensity was observed. The intensity change at a forbidden nuclear position was followed in Fig. 1(b) to track the onset of magnetic ordering. This indicated a magnetic ordering below $T_N=80$ K, consistent with the SQUID data [8]. The same magnetic reflections were present at 65 K, 40 K, and 4 K with no change indicative of further magnetic transitions within the resolution of the present measurements. Further measurements on single crys-

tals or with higher resolution will be of interest to probe these subtle changes observed in Ref.[8].

A propagation vector of $\mathbf{k} = (\frac{1}{2}, \frac{1}{2}, 0)$ was determined from the positions of the magnetic reflections. Using the Bilbao Crystallographic Server and non-magnetic space group $P2_1/n$ (non-standard setting) with the determined \mathbf{k} -vector gives the P_S-1 (#2.7) magnetic space group as the only maximally allowed structure with non-zero moments. The direction of the moments is unconstrained in this model. Given the number of variables, powder averaging inherent in the data and small contribution from the Ir ion we attempted to limit the spin directions to uncover the dominant component. Confining the spins to the a -axis produced the most reasonable agreement of any of the trial a, b, c directions to the data with an R_{mag} value of 22.1. Allowing the spins to have a component along the c -axis further increased the agreement to the data with an R_{mag} value of 6.25. This model is shown in Fig. 1(d). When the moments were allowed to freely refine along all directions the b -axis produced a value with a large error within zero, distinct from the a and c axis. As such we present a magnetic model for $\text{La}_2\text{NiIrO}_6$ with only a - c spin components, however we cannot rule out a b -axis component. The refined moment values in our model were $1.53(5)\mu_B/\text{Ni}^{2+}$ with components $(m_a, m_b, m_c) = (1.0, 0, 1.1)$ and $0.17(3)\mu_B/\text{Ir}^{4+}$ with components $(m_a, m_b, m_c) = (0.12, 0, 0.13)$. We note that the low moment of Ir^{4+} is beyond the typical limit for this measurement and therefore is presented as the best fit model. The errors from the Rietveld refinement are likely an underestimation and we cannot rule out the Ir^{4+} having a zero moment or the Ir and Ni sublattices ordering at different temperatures. Further measurements sensitive to the Ir ion, such as resonant x-ray scattering, would be of interest, as would measurements on crystals to determine the spin direction of all the moments.

2. $\text{Nd}_2\text{NiIrO}_6$

	x	y	z	Site
Nd	0.015(2)	0.565(1)	0.565(1)	4e
Ir	0	0	0	2a
Ni	0	0	0.5	2b
O1	0.099(2)	0.029(2)	0.267(3)	4e
O2	0.184(4)	0.283(5)	-0.057(3)	4e
O3	0.202(4)	0.312(5)	0.548(4)	4e

TABLE II. Crystal structure of $\text{Nd}_2\text{NiIrO}_6$ at 150 K from neutron refinement in the $P2_1/n$ space group with $a=5.429(7)\text{\AA}$, $b=5.682(7)\text{\AA}$, $c=7.753(9)\text{\AA}$, $\beta=90.17(2)^\circ$.

We now turn to the compositions with magnetic $3d$ - $5d$ - $4f$ ions. $\text{Nd}_2\text{NiIrO}_6$ was reported to have a ferromagnetic-like transition around 125 K with a further anomaly at 6 K consistent with antiferromagnetic interactions, based on SQUID measurements [8]. To follow the magnetic structure we therefore collected neutron diffraction measurements at 4, 40, and 150 K. The high temperature measurement, shown in Fig. 2(a) and Table II, was used to confirm purity and obtain a non-magnetic structural model in the paramagnetic regime. This

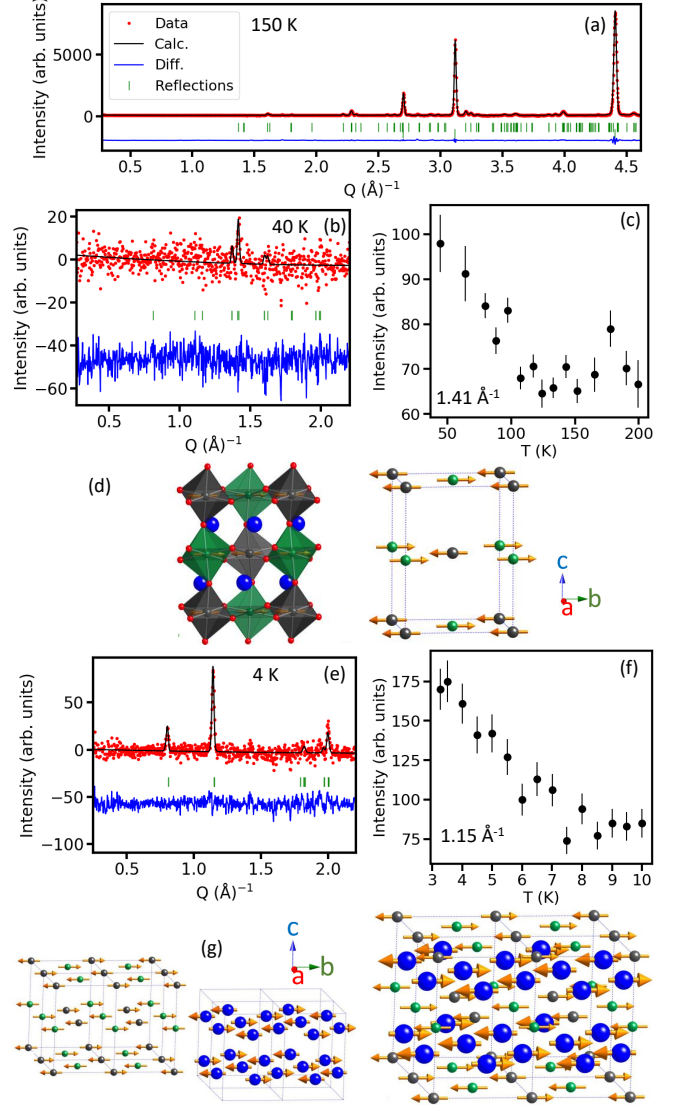


FIG. 2. Magnetic structure of $\text{Nd}_2\text{NiIrO}_6$. (a) Refinement of the 150 K neutron diffraction pattern to the crystal structure (upper reflections). Lower reflections correspond to Al sample holder scattering. (b) Magnetic structure model obtained by subtracting the 150 K neutron pattern from the 40 K data. (c) Intensity of the reflection at 1.41 \AA^{-1} as a function of temperature. (d) 40 K magnetic structure model with Nd (blue), Ni (green) and Ir (grey) atoms shown. (e) Magnetic structure model obtained by subtracting the 150 K neutron pattern from the 4 K data. (f) Intensity of the reflection at 1.15 \AA^{-1} as a function of temperature. (g) 4 K magnetic structure for Ni/Ir ions (left), Nd ions (middle) and all magnetic ions (right). One magnetic unit cell is shown with the dashed lines correspond to the non-magnetic unit cell.

was refined with the $P2_1/n$ space group. The 40 K measurement revealed additional scattering, which is shown in Fig. 2(b) where the 150 K data has been subtracted from the 40 K data. The intensity of the scattering at 1.41 \AA^{-1} was followed as a function of temperature, see Fig. 2(c). The increase in intensity is consistent with the predicted magnetic ordering at 125 K from bulk data [8]. The additional scat-

tering could be indexed to a propagation vector of $k = (0, 0, 0)$. Given this k vector and $P2_1/n$ symmetry of the nuclear structure gives four maximally allowed magnetic space groups: $P2'_1/c'(\#14.79)$, $P2_1/c'(\#14.78)$, $P2'_1/c(\#14.77)$ and $P2_1/c(\#14.75)$. Magnetic space groups $\#14.77$ and $\#14.78$ only allow moments on the Nd ion and could be discarded. The remaining two magnetic space groups do not constrain the moments to any fixed axis. The best fit to the data was obtained with a ferrimagnetic arrangement of Ni and Ir in the b axis in the magnetic space group $P2_1/c(\#14.75)$. Magnetic moments of $1.71(2)\mu_B$ (Ni) and $0.32(7)\mu_B$ (Ir) were determined, corresponding to R_{mag} of 25.7. The higher agreement index of this fit compared to previous refinements is due to the weaker intensity and reduced number of the magnetic reflections in this phase. Attempts to improve this R_{mag} by introducing components away from the b -axis did not appreciably improve the fit. A ferromagnetic model is additionally in agreement with the data, however the ferrimagnetic model presented is more consistent with bulk measurements previously reported [8]. We note again that the low moment of Ir^{4+} is beyond the typical limit for this measurement and therefore is presented as the best fit model.

Upon cooling to 4 K, additional magnetic reflections appeared in the diffraction pattern, shown in Fig. 2(e) for the difference between the 4 K data and the 150 K data. The intensity at the most intense reflection position was followed as a function of temperature in Fig. 2(f). This revealed the onset of magnetic ordering below 7 K, consistent with reported SQUID results [8]. The magnetic reflections observed at 4 K were indexed to a $k=(\frac{1}{2}, \frac{1}{2}, 0)$ propagation vector within the non-magnetic space group $P2_1/n$. Only one maximal magnetic space group allows moments for Ni/Ir, as well as Nd: P_S-1 . A magnetic model with the spins still confined to the b -axis but in an antiferromagnetic arrangement for all the ions yields the best fit to the data. Magnetic moments of $2.20(4)\mu_B/\text{Nd}^{3+}$, $1.27(4)\mu_B/\text{Ni}^{2+}$ and $0.32(5)\mu_B/\text{Ir}^{4+}$ were determined.

The magnetic behavior of $\text{Nd}_2\text{NiIrO}_6$ upon cooling is therefore characterized as first undergoing ferrimagnetic ordering of the Ni/Ir ions with the magnetic order keeping the unit cell size unaltered. Then only at the low temperature of 7 K does the Nd ion order along with a change in the ordering of the Ni/Ir magnetic order to antiferromagnetic to create a magnetic unit cell doubled in size along the a and b axis.

3. $\text{Pr}_2\text{NiIrO}_6$

The composition $\text{Pr}_2\text{NiIrO}_6$ was measured at 1.5, 20, 75, and 125 K temperatures to follow anomalies observed in previous SQUID measurements [8]. These indicated ferromagnetic-like ordering at 105 K with a further transition at 5 K. The high temperature 125 K neutron diffraction measurement shown in Fig. 3(a) was used to confirm sample purity and the $P2_1/n$ structural model in the paramagnetic regime, see Table III. Upon cooling below 110 K, additional Bragg reflections appeared. This is shown in Fig. 3(b) by following the intensity at 1.41 \AA^{-1} . Figure 3(c)

	x	y	z	Site
Pr	0.012(3)	0.560(1)	0.754(5)	4e
Ir	0	0	0	2a
Ni	0	0	0.5	2b
O1	0.094(1)	0.026(1)	0.263(2)	4e
O2	0.186(3)	0.296(4)	-0.057(1)	4e
O3	0.198(3)	0.290(4)	0.532(2)	4e

TABLE III. Crystal structure of $\text{Pr}_2\text{NiIrO}_6$ at 150 K from neutron refinement in the $P2_1/n$ space group with $a=5.473(2)\text{\AA}$, $b=5.661(3)\text{\AA}$, $c=7.790(3)\text{\AA}$, $\beta=90.03(2)^\circ$.

shows all the observed magnetic reflections by subtracting the 125 K data from the 20 K data. There was no difference between the 20 K and 75 K measurements apart from increased intensity of the new magnetic reflections at the lower temperature measurement. Both temperatures have a $k = (0, 0, 0)$ propagation vector. The scattering is similar to that observed for the $\text{Nd}_2\text{NiIrO}_6$ 20 K measurement, however here in the $\text{Pr}_2\text{NiIrO}_6$ case the signal to noise is improved and additional weaker reflections were observed. Following an identical analysis described above the magnetic space group of $P2_1/c(\#14.75)$ used for $\text{Nd}_2\text{NiIrO}_6$ was found to best fit the $\text{Pr}_2\text{NiIrO}_6$ data at 20 K, shown in Fig. 3(c). The magnetic spins are primarily along the b -axis, however to model all the magnetic reflections a component along the a -axis needed to be added. This gives the ferrimagnetic structure shown in Fig. 3(f) with the Ni ions ordered ferromagnetically and the Ir ions ordered ferromagnetically. Magnetic moments of $1.61(4)\mu_B/\text{Ni}^{2+}$ with components $(m_a, m_b, m_c) = (0.6, 1.5, 0)$ and $0.34(8)\mu_B/\text{Ir}^{4+}$ with components $(m_a, m_b, m_c) = (0.1, 0.3, 0)$ are found. Again the small moment size for Ir is presented as a best fit model and we cannot rule out a zero ordered moment.

Cooling further from 20 K to 1.5 K additional magnetic scattering is observed as new intensity at certain reflections, while other positions such as at 1.38 \AA^{-1} and 1.41 \AA^{-1} , remain unchanged. The intensity change at 1.96 \AA^{-1} is shown in Fig. 3(d). Figure 3(e) shows all the observed magnetic reflections at 1.5 K by subtracting the 125 K data from the 1.5 K data. The propagation vector is also unchanged from the high temperature phase, $k = (0, 0, 0)$. This behavior is consistent with the ordering of the Pr ion while the Ni/Ir ions magnetic order remains unchanged. A clear contrast is observed with the $\text{Nd}_2\text{NiIrO}_6$ composition that showed a change in the Ni/Ir ordering at the low temperature magnetic phase transition. To model the 1.5 K data for $\text{Pr}_2\text{NiIrO}_6$ we keep the same magnetic space group of $P2_1/c(\#14.75)$ and include a moment on the Pr ion. The data refined to having the Pr ion in the ab -plane in a ferromagnetic arrangement similar to the Ni/Ir ions. The refinement to the 1.5 K data with the 125 K data subtracted is shown in Fig. 3(e) and the corresponding spin model in Fig. 3(g). The best fit model corresponds to magnetic moments of $1.63(4)\mu_B/\text{Ni}^{2+}$ with components $(m_a, m_b, m_c) = (0.6, 1.5, 0)$ and $0.39(7)\mu_B/\text{Ir}^{4+}$ with components $(m_a, m_b, m_c) = (0.1, 0.3, 0)$ and $1.58(3)\mu_B/\text{Pr}^{3+}$ with components $(m_a, m_b, m_c) = (1.0, 1.2, 0)$.

The onset of Pr ordering therefore contributes to the over-

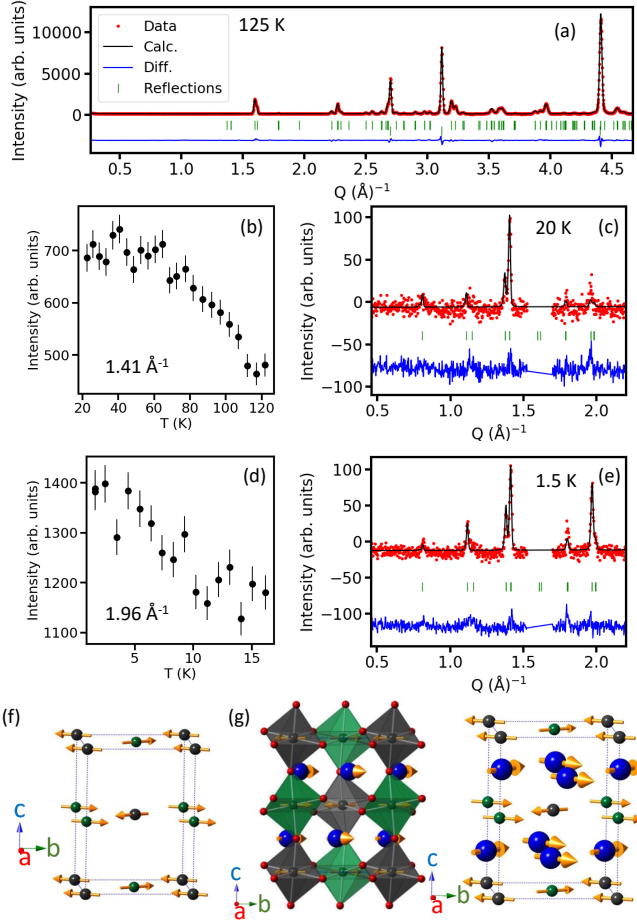


FIG. 3. Magnetic structure of $\text{Pr}_2\text{NiIrO}_6$. (a) Refinement of the 125 K neutron diffraction pattern to the crystal structure (upper reflections). Lower reflections correspond to Al sample holder scattering. (b) Intensity of the reflection at 1.41 \AA^{-1} as a function of temperature. (c) Magnetic structure model obtained by subtracting the 125 K neutron pattern from the 20 K data. Scattering around 1.6 \AA^{-1} due to the strong nuclear contribution. (d) Intensity of the reflection at 1.96 \AA^{-1} as a function of temperature. (e) Magnetic structure model obtained by subtracting the 125 K neutron pattern from the 1.5 K data. Scattering around 1.6 \AA^{-1} due to the strong nuclear contribution. (f) Magnetic-atom only representation of the magnetic structure at 20 K of $\text{Pr}_2\text{NiIrO}_6$ showing, Ni (green) and Ir (black) ions. The unit cell is outlined with the blue dashed line. (g) Polyhedral representation of the magnetic (1.5 K) and nuclear structure of $\text{Pr}_2\text{NiIrO}_6$ and magnetic-atom only representation of the 1.5 K magnetic structure of $\text{Pr}_2\text{NiIrO}_6$ showing Pr (blue), Ni (green) and Ir (black) magnetic ions.

all ferrimagnetic ordering within $\text{Pr}_2\text{NiIrO}_6$, with the Pr $1.58(3)\mu_B$ ordering ferromagnetically along the b axis in a zig-zag fashion due to a spin angle of $48.1(1)^\circ$ off the b axis. The best fit model indicates the Pr and Ni ordering with the spins in the same direction along the b-axis and the Ir in the opposite direction. Further measurements on single crystals and with elemental specific analysis available with resonant x-ray scattering will be of interest to test this model and contrast it against a fully ferromagnetic ordering of all three magnetic

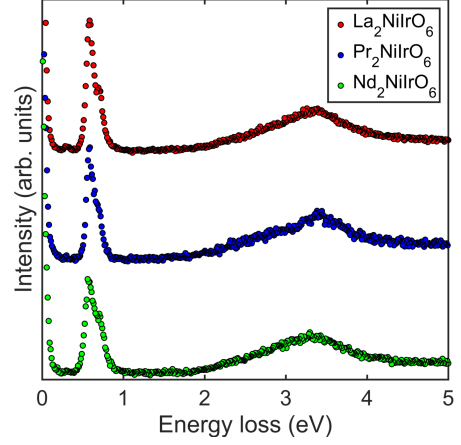


FIG. 4. Resonant inelastic x-ray scattering measurements of powder $\text{Ln}_2\text{NiIrO}_6$ ($\text{Ln} = \text{La}, \text{Pr}, \text{Nd}$) at 5 K on the MERIX spectrometer. The incident energy was 11.215 keV corresponding to the Ir L_3 -edge. The data have been offset by a constant factor for clarity.

ions.

B. RIXS measurements of SOC-Induced t_{2g} manifold splitting

To gain insight into the electronic ground state of the Ir^{4+} ($5d^5$) ion in $\text{Ln}_2\text{NiIrO}_6$ RIXS measurements were performed. The energy was tuned to 11.215 keV corresponding to the Ir L_3 -edge which allows for an isolation of the Ir scattering. The 5 K data is shown in Fig. 4. No change was observed in measurements collected at higher temperatures. Each compounds spectra consisted of two main features around 0.6 eV and 3.5 eV. The spectra are consistent with similar octahedrally coordinated Ir^{4+} ion and provides all the signatures of a SOC split $J_{\text{eff}} = \frac{1}{2}$ state [57, 58]. The broad, higher energy (3.5 eV) peak corresponds to $d-d$ excitations from transitions between the t_{2g} and e_g orbitals, which are split because of the crystal field. The sharper, lower energy scattering consists of two separate peaks, within the 35 meV resolution of the instrument. This scattering can be assigned to $d-d$ excitations from intraband t_{2g} transitions due to the splitting of the t_{2g} manifold into a $J_{\text{eff}} = \frac{1}{2}$ and $J_{\text{eff}} = \frac{3}{2}$ state, characteristic of many complex iridates [40]. By fitting these reflections to simple Gaussian peaks we extract peak energies as: $\text{La}_2\text{NiIrO}_6 = 0.60(2)$ eV and $0.71(2)$ eV; $\text{Pr}_2\text{NiIrO}_6 = 0.58(1)$ eV and $0.65(1)$ eV; $\text{Nd}_2\text{NiIrO}_6 = 0.59(2)$ and $0.71(3)$ eV. The presence of two resolvable peaks is consistent with a small departure from an ideal $J_{\text{eff}} = \frac{1}{2}$ state due to the distortions inherent in the crystal structure that is observed in all reported Ir materials in the literature [57, 58]. The singular unpaired electron present in the $J_{\text{eff}} = \frac{1}{2}$ level for $5d^5 \text{Ir}^{4+}$ is commonly observed as possessing a significantly reduced magnetic moment, such as that observed in $\text{Ln}_2\text{NiIrO}_6$ reported above of $\sim 0.3\mu_B$, further supporting a $J_{\text{eff}} = \frac{1}{2}$ state.

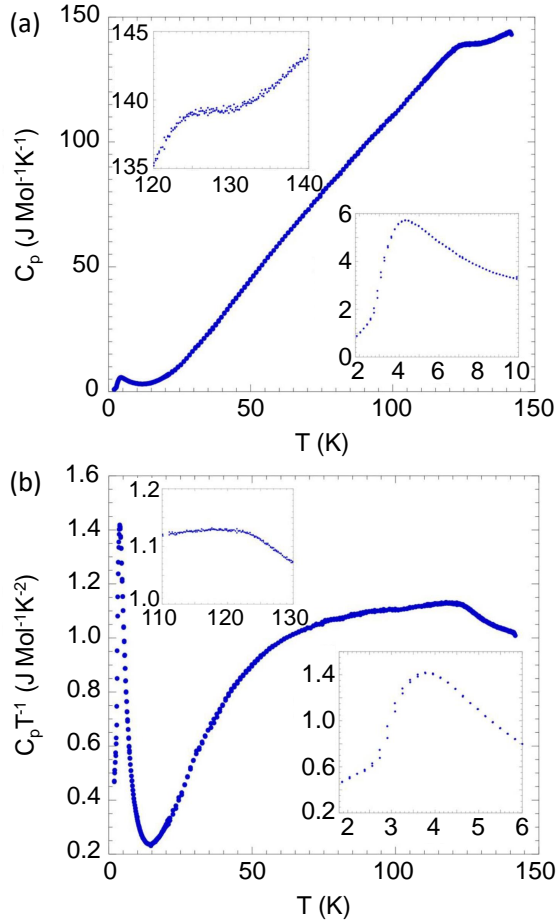


FIG. 5. (a) Bulk heat capacity (C_p) for $\text{Pr}_2\text{NiIrO}_6$ in zero field. The onset of Ni/Ir ordering is shown more clearly in the upper left inset, and the onset of Pr ordering is shown in the bottom right inset. (b) Bulk heat capacity divided by temperature (T) plotted against temperature for $\text{Pr}_2\text{NiIrO}_6$.

C. Heat Capacity, electrical resistivity and DFT investigations of $\text{Pr}_2\text{NiIrO}_6$

1. Heat Capacity of $\text{Pr}_2\text{NiIrO}_6$

Heat capacity measurements were undertaken on a pressed and sintered pellet of $\text{Pr}_2\text{NiIrO}_6$, shown in Fig. 5(a), to further investigate the long-range ordering and probe for independent Pr and Ni/Ir magnetic sublattices. Two clear transitions are observed at 123 K and 3.7 K, confirming the nature of long-range ordering temperatures. The broadness of the high temperature transition may be due to thermal fluctuation, a product of measuring at high temperature, or may be due to poor sintering of this sample. In addition we cannot rule out this as indicating low dimensional correlations for one or more of the ions. This transition was further resolved by plotting heat capacity (C_p) divided by temperature (C_p/T) against temperature, shown in Fig. 5(b). Although broad features are still present, the 123 K transition is clear. As this transition is consistent with both neutron and susceptibility measurements

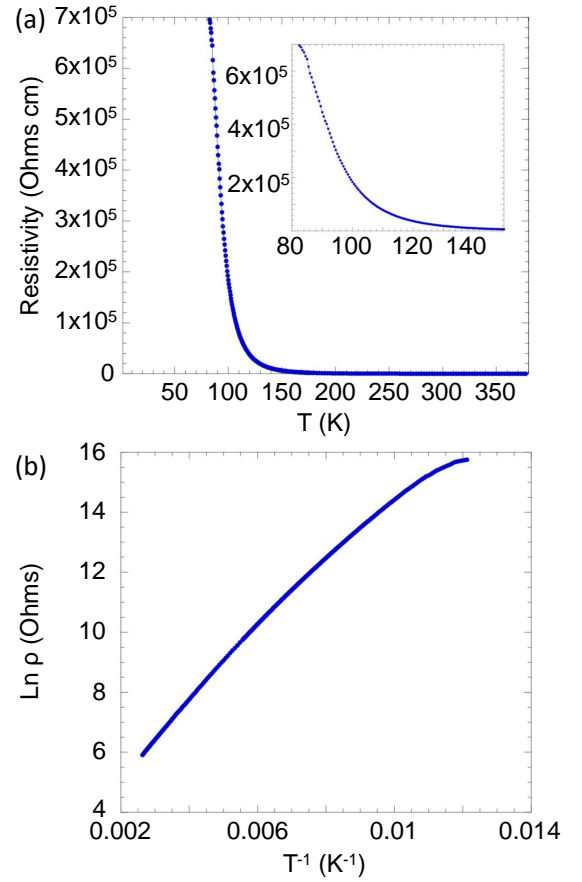


FIG. 6. (a) Temperature dependence of the electrical resistivity for $\text{Pr}_2\text{NiIrO}_6$. The inset depicts that resistivity was not measured below 82.5 K due to instrumental limits of Ohms-cm capability. (b) Inverse temperature dependence of the natural logarithm of resistance for $\text{Pr}_2\text{NiIrO}_6$. Linearity for the case of T - n , such that $n = 1$, indicates thermally activated conduction.

indicating the onset of ferromagnetic-like order, its magnetic origin corresponds to the onset of Ni/Ir magnetic ordering. Interestingly, the transition at 3.7 K was found to be sharp and lambda-like, and is consistent with the small transition observed in zero-field cooled measurements shown in Fig. 5(b) and the 1.5 K powder neutron diffraction data, suggesting the onset of Pr magnetic ordering. A small change in slope of heat capacity data can be observed below 2.7 K, but the nature of this transition is unclear. Based on the neutron and susceptibility data measurements, it does not correspond to any long range nuclear or magnetic order, suggesting possible crystal field effects between the three present magnetic ions in this structure.

2. Electrical Resistivity of $\text{Pr}_2\text{NiIrO}_6$

Temperature dependent electrical resistivity measurements for $\text{Pr}_2\text{NiIrO}_6$ are shown in Fig. 6(a). The sharp decrease in resistance as a function of increasing temperature indicates

that the material is not metallic. Considering low measured resistance of 37 Ohms-cm at 380 K, especially for oxide materials [59], semiconducting behavior is possible. This was further investigated by assessing the conduction mechanism via plotting the natural logarithm of resistance against T^{-n} , such that the value of n indicates the dimensionality and type of transport mechanism. For values of $n = 1$, linearity indicates a simple thermally activated conduction pathway, whereas values for n greater than 1 indicate a Mott variable range hopping mechanism of variable dimensionality. Fig. 6(b) depicts near perfect linearity is exhibited for $n = 1$, indicating the conduction pathway is thermally mediated.

3. First Principles Calculations for $\text{Pr}_2\text{NiIrO}_6$

In an attempt to better understand the complex magnetic behavior for $\text{Pr}_2\text{NiIrO}_6$, we have performed first principles calculations of the magnetic order and energetics. Given both the complex monoclinic physical structure as well as the non-collinear canted magnetic structure, with effectively 3 different magnetic ions (the dominant Ni, less dominant Pr, and induced moment Ir), we make certain simplifications in order to render the problem computationally and analytically tractable. First, we consider only collinear states. While the actual observed ground state in $\text{Pr}_2\text{NiIrO}_6$ is not collinear, a detailed examination of Fig. 3(f) (Ni/Ir ordering) and Fig. 3(g) (all ions order) shows that deviations of the respective magnetic ions from collinearity are less than 30° off the b axis for both Ni and Ir, but is a bit more significant for Pr.

Given the monoclinic symmetry, there is a large manifold of potential exchange interactions, with several potential nearly-“nearest-neighbor” interactions, with slightly variable distances between Ni and Ni, Ni and Pr, Pr and Pr, and these atoms with Ir. To simplify matters we consider only Ni-Ni, Ni-Pr and Pr-Pr effective exchange interactions and consider the several nearly degenerate distances in each of these categories into one interaction for each category. We note in passing that it is not surprising that this compound exhibits a complex non-collinear magnetic structure in view of the complex physical structure and the three effectively magnetic ions, along with the disparate spin-orbit energy scales of Ni (~ 50 meV), Pr (~ 0.5 eV), and Ir (~ 1 eV). Note that the Ir atom is explicitly included in the DFT calculations themselves but for simplicity is not included in the extraction of exchange constants as this would substantially complicate the analysis.

For the purposes of determining the ground state and associated excited state energetics, five distinct magnetic arrangements were considered. We show in Fig. 7 — a configuration with Ni-Ni and Pr-Pr near-neighbor pairs antialigned (Ni_AF_Pr_AF). We considered four additional arrangements, including a ferromagnetic state (FM) and three more complex arrangements. For these purposes spin-orbit coupling was omitted, though for a detailed examination of the FM ground state below we include it. Here a crystallographic unit cell contains 2 formula units. The arrangements considered, in addition to the ferromagnetic case, were as follows: a state with Ni and Pr antiparallel to each other — a fer-

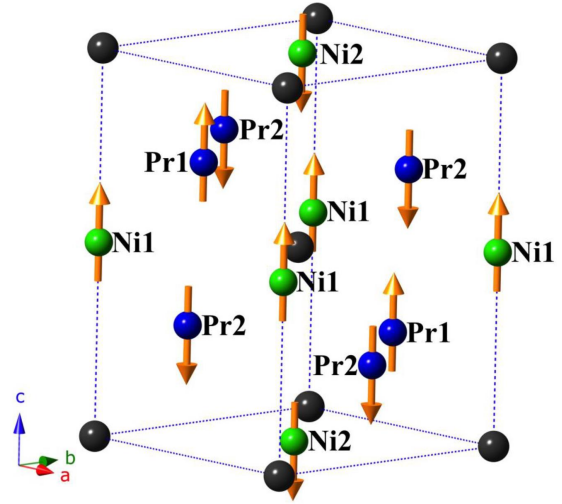


FIG. 7. A depiction of the primary magnetic moment-bearing atoms described within the first principles calculations. Praseodymium atoms are depicted as blue spheres, Nickel atoms as green spheres, and Iridium atoms as dark grey spheres (no label), as indicated. For clarity, all spheres are shown as the same size, regardless of atomic size. The “Ni_AF_Pr_AF” state is shown above. For the “FM” state, all Ni and Pr atoms are ferromagnetically coupled. For “Ni_Pr_FI”, the Ni and Pr atoms are antiferromagnetically coupled. For “Ni_AF_Pr_FM”, the Ni1 and Ni2 atoms are antiferromagnetically coupled while all Pr atoms are ferromagnetically coupled to Ni1. For “Ni_FM_Pr_AF”, Ni1 and Ni2 are ferromagnetically coupled while Pr1 is ferromagnetically coupled to Ni1 and Ni2 while Pr2 is antiferromagnetically coupled to Ni1 and Ni2. For “Ni_AF_Pr_AF”, Ni1 and Ni2 are antiferromagnetically coupled and Pr1 and Pr2 are also antiferromagnetically coupled. Note that the *apparent* fourfold Pr2 falls on the a -face zone boundary (unlike Pr1, which is within the cell), so that there are only two Pr2 per unit cell. Similarly, the four Ni1 atoms fall on the zone edge, so that there is only one Ni1 per unit cell, and the two Ni2 atoms fall on the c -face zone boundary. The vertical moment orientation is for clarity of presentation; moment orientation was not studied in these calculations.

romagnetic state (Ni_Pr_FI; total moment $6 \mu_B/\text{u.c.}$), a state with the two unit cell Ni antiparallel, with the Pr themselves aligned (Ni_AF_Pr_FM, total moment $7.82 \mu_B/\text{u.c.}$); a state with the 2 Ni ferromagnetically coupled, but 2 of the 4 Pr anti-aligned to the other 2; (Ni_FM_Pr_AF, total moment $2 \mu_B/\text{u.c.}$) and a state with the 2 Ni antiferromagnetically coupled, and 2 of the 4 Pr antiferromagnetically coupled to the other two (Ni_AF_Pr_AF, no net moment). Note that of these last 4 states, only the last is truly a zero-moment antiferromagnetic state. In general, individual spin moment magnitudes within these several magnetic states are generally fairly rigid, with little variation ($< 3\%$) between states; typical values, in the absence of spin-orbit coupling and thereby orbital moments, are $1.96 \mu_B/\text{Pr}$ and $1.29 \mu_B/\text{Ni}$. Details are given in Table IV. We will see below that despite the smaller moment and fewer atoms per cell, it is the Ni atoms that are ultimately dictating most of the magnetic character, due to the generally much larger spatial extent of the Ni $3d$ wavefunctions, relative to the Pr $4f$ wavefunctions, which are much

State	Energy relative to FM GGA	Energy relative to FM GGA+ U (per u.c.)	Total Spin Moment (μ_B /u.c., GGA+U)
FM	0.0	0.0	10.0
Ni_Pr_FI	49.56	41.96	6.0
Ni_AF_Pr_FM	51.41	114.86	7.82
Ni_FM_Pr_AF	103.48	37.68	2.0
Ni_AF_Pr_AF	86.38	86.40	0.0

TABLE IV. Detailed magnetic properties of several magnetic configurations of $\text{Pr}_2\text{NiIrO}_6$ studied within density functional theory. The configurations' relative orientation of the Ni and Pr spin magnetic moments are described in the text.

more localized in the Pr core.

We see that from Table IV, the state with the 2 Ni atoms antiferromagnetically coupled, but the Pr ferromagnetically coupled, is the highest energy state in this manifold, nearly 115 meV/u.c. above the ferromagnetic ground state, while the reverse (Ni_FM_Pr_AF) is only 37.7 meV/u.c. above. This accords with our intuitive expectation that Ni-Ni exchange interactions should be stronger than Pr-Pr exchange interactions, but what is surprising is that this is the case even though the Ni-Ni nearest neighbor distances are of the order of 5.7 Å whereas those for Pr are only of order 4.1 Å. This is reflective both of the general localization of the Pr 4f electrons within the core, away from the Fermi level, and also of recent findings in $\text{Cr}_{1/3}\text{NbS}_2$ [60] where exchange interactions mediated through electronegative elements can be much more long range than would commonly be expected. Quantitatively, mapping the above energetics to a Heisenberg model (appropriate in view of the rigidity of the moments) finds Ni-Ni, Ni-Pr and Pr-Pr exchange interactions of -4.32, -3.18 and -0.58 meV, (all ferromagnetic) respectively, confirming the expectation for the dominance of the Ni magnetic interaction here. In particular, the Pr-Pr exchange interaction is relatively weak and confirms our general expectation that the Pr 4f electrons are localized in the core and do not interact strongly with other Pr atoms, reducing the Pr ordering temperature.

Also evident from Table IV are substantially altered energetics in the “straight GGA” calculations, in which no Hubbard U is applied to Pr. The exchange energetics change considerably; for example, the Ni_FM_Pr_AF state in the straight GGA is now 103.48 meV/u.c. above the ferromagnetic state, whereas in the GGA+U it is just 37.68 meV/u.c. above the unit cell, and this state now falls considerably higher (62 meV/u.c.) in energy above the Ni_AF_Pr_FM state where it is some 77 meV/u.c. lower in the GGA+U. Most strikingly, extracting from these energetics the Ni-Ni, Ni-Pr and Pr-Pr exchange interactions, one now finds the Pr-Pr exchange interaction predominant in magnitude at -8.65 meV, with the Ni-Pr exchange at -4.05 meV and the Ni-Ni much smaller at just -0.06 meV. Thus the straight GGA would here inaccurately claim the Pr-Pr magnetic interaction to be the predominant one, a logical consequence of the GGA's placing the Pr 4f orbitals at or near the Fermi level, where they interact strongly with other atoms, instead of being properly localized in the

core of the Pr atom, as a wealth of experience with rare earth ions dictates. Thus the application of a substantial U value (here chosen as 5 eV) is critical to a proper description of the magnetism in this compound.

As mentioned previously, we now give a more complete description of the FM ground state with spin-orbit coupling included for all atoms with the GGA+U approach. This changes both the total spin moment significantly (it increases to 10.68 μ_B /u.c.) and adds significant orbital moment contributions. In particular, Pr exhibits a large negative orbital moment of -0.795 μ_B , while Ni acquires a significant orbital moment of 0.087 μ_B , and Ir also has a significant negative orbital moment of -0.197 μ_B . This yields total moments for these three atoms of 1.17 μ_B , 1.45 μ_B , and -0.35 μ_B with a unit cell total of 7.28 μ_B , or 3.64 μ_B /f.u. The above values are comparable to the experimental values of 1.58(3) μ_B for Pr, 1.63(4) μ_B for Ni, and 0.39(7) μ_B for Ir. It is of interest that the largest orbital moment magnitudes are for the heavy atoms (Pr and Ir), corresponding to the generally stronger spin-orbit coupling in these atoms, as well as the localized nature of the Pr 4f states. The addition of spin-orbit also changes the Iridium spin-moment from -0.30 μ_B to a value half this, suggesting the particular relevance of spin-orbit coupling here, as evidenced experimentally in the RIXS measurements discussed above.

It is of interest both that the Iridium atom couples antiferromagnetically to the Pr and Ni atoms and that its spin moment is significantly reduced by the application of spin-orbit coupling. Sitting at the center of a distorted Oxygen octahedron, its antiferromagnetic coupling is notable in view of the ferromagnetic coupling of Ni itself, sitting near the center of a similar Oxygen octahedron. It is also remarkable that its orbital moment of -0.197 μ_B is significantly larger in magnitude than its spin moment of -0.15 μ_B , and this may be understood in terms of its spin-orbit energy scale of ~ 1 eV effectively outstripping its exchange interaction energy scales, which may be expected to be much smaller than the predominant Ni-Ni exchange interaction. Note that the Ir orbital and spin moments are parallel, in accordance with Hund's rules. It is likely that the Oxygen atoms intervening between the Ni and Ir atoms cause a predominant antiferromagnetic superexchange interaction between these atoms. The Ir atom thus likely plays an important role in the overall Ni-Ni magnetic exchange interaction, despite carrying a comparatively small moment itself. The total calculated Ir moment of 0.35 μ_B is consistent both with the neutron-found value of ~ 0.3 μ_B and with the $J=1/2$ state inferred from the RIXS measurements.

To further relate these results to the RIXS data we present in Figure 8 the calculated density-of-states (DOS), within the modeled ferromagnetic state, with spin-orbit coupling in the GGA+U. For simplicity we present only the majority spin (or spin-up) DOS and focus on the RIXS-relevant region around the Fermi level. One immediately notes the presence of substantial, in fact predominant Ir character (blue dotted line) in the region within half an eV of E_F . Furthermore, we note two Ir-generated DOS peaks falling approximately -0.25 below and 0.15 eV above E_F . It is quite likely that 0.4 eV transitions between these regions correspond to the Ir intraband t_{2g} transitions observed at ~ 0.6 eV in the RIXS, with the differ-

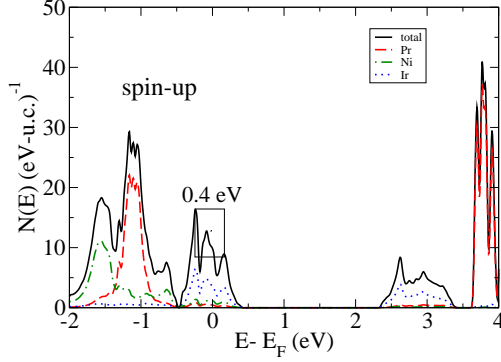


FIG. 8. The calculated spin-up density-of-states of $\text{Pr}_2\text{NiIrO}_6$ in the modeled ferromagnetic groundstate, within GGA+U with spin-orbit coupling applied. Note the RIXS-relevant transition indicated around the Fermi level, indicative of the intraband Ir transition found in RIXS

ence in energies (0.4 vs. 0.6 eV) reasonably ascribed to our simplified treatment of the magnetism in this system.

It is also possible to relate the above GGA+U energetics to the observed ordering points of the Ni and Pr atoms, which significantly differ in temperature. In an approximation where the ordering point of a magnetic atom, in a local moment approximation, is estimated at 1/3 the energy difference, per magnetic atom, [55, 61, 62], between configurations with that atom ferromagnetically and antiferromagnetically coupled to the remainder of the system, we use the Ni_FM_Pr_AF state for the Pr atom (relative to the FM ground state) and, correspondingly, the Ni_AF_Pr_FM for the Ni atom, accounting for the different multiplicity of these atoms, and obtain estimated ordering points for the Pr and Ni atoms as 36 and 222 K. While these are somewhat higher than the actual values (due to our wholesale neglect of fluctuations, among other factors), their relative magnitudes are in accordance with the experimental facts. In particular, as seen in experiment, the Nickel atoms are driving the magnetism, despite their roughly equivalent local moment and substantial nearest-neighbor distances. This mainly reflects the spatially extended nature of the $3d$ states associated with the Ni atom magnetism and the generally core-localized nature of the Pr $4f$ electrons associated with the Pr magnetism.

IV. CONCLUSIONS

A series of double perovskite iridates of the formula $\text{Ln}_2\text{NiIrO}_6$ were investigated using thermodynamic and transport properties, neutron powder diffraction, RIXS, and DFT calculations to elucidate the role superexchange plays in hybrid $3d$ - $5d$ - $4f$ compositions with variable A-site cations. The composition $\text{La}_2\text{NiIrO}_6$ was determined to be a non-collinear antiferromagnet in the ac -plane with the ordering of Ni/Ir occurring simultaneously. For $\text{Nd}_2\text{NiIrO}_6$ two distinct magnetic structures were determined. The first high temperature

magnetic phase consists of ferromagnetically ordered Ni/Ir sublattices creating a ferrimagnetic structure primarily along the b -axis. Cooling $\text{Nd}_2\text{NiIrO}_6$ led to a magnetic structure change where the Nd ion orders and the Ni/Ir ordering also changes into a AFM Ni/Ir sublattices. Two independent magnetic sublattices (Pr and Ni/Ir) were found in the composition $\text{Pr}_2\text{NiIrO}_6$, corresponding to ab -plane ferrimagnetic order between Ni and Ir, and a zig-zag ferromagnetic order of Pr along the b -axis, resulting in an overall ferrimagnetic order. The presence of two independent magnetic sublattices was corroborated by heat capacity measurements, demonstrating transitions at 123 K (Ni/Ir ordering) and 3.7 K (Pr ordering). Resistivity measurements indicated semiconducting behavior and thermally mediated conduction for $\text{Pr}_2\text{NiIrO}_6$. DFT results confirm the independent sublattice ordering and demonstrate the primacy of the Ni atom in determining the magnetic character, despite the Ni-Ni nearest-neighbor distances of some 5.7 Å. All compositions were measured with RIXS, confirming that spin-orbit coupling splits the t_{2g} manifold of octahedral Ir^{4+} into a $J_{\text{eff}} = \frac{1}{2}$ and $J_{\text{eff}} = \frac{3}{2}$ state. Collectively the results demonstrate the dramatic changes in magnetic ordering that can be induced within structurally similar $3d$ - $5d$ - $4f$ compounds as the Ln ion is varied and as different temperature regimes are accessed. As shown in the DFT calculations and experimental data the presences of distinct magnetic ions with a spectrum of SOC strength and orbital overlaps leads to the inducing of magnetic interactions that otherwise would not occur and goes beyond predictions that apply to simpler systems less magnetic ions, such as the Kanamori-Goodenough rules. This motivates further investigations into hybrid materials with multiple magnetic ions.

ACKNOWLEDGMENTS

This research used resources at the High Flux Isotope Reactor, a DOE Office of Science User Facility operated by the Oak Ridge National Laboratory. This work was partly supported by the U.S. Department of Energy (DOE), Office of Science, Office of Workforce Development for Teachers and Scientists, Office of Science Graduate Student Research (SCGSR) program. The SCGSR program is administered by the Oak Ridge Institute for Science and Education for the DOE under contract number DE-SC0014664. Research at Oak Ridge National Laboratory (ORNL) was supported by the DOE, Office of Science, Basic Energy Sciences (BES), Materials Science and Engineering Division. Sample synthesis and structural characterization performed at the University of South Carolina were supported by the National Science Foundation under Awards DMR-1301757 and DMR-1806279. This work used resources of the Advanced Photon Source, an Office of Science User Facility operated for the U.S. DOE Office of Science by Argonne National Laboratory. This manuscript has been authored by UT-Battelle, LLC under Contract No. DE-AC05-00OR22725 with the U.S. Department of Energy. The United States Government retains and the publisher, by accepting the article for publication, acknowledges that the United States Gov-

ernment retains a non-exclusive, paidup, irrevocable, world-wide license to publish or reproduce the published form of this manuscript, or allow others to do so, for United States Government purposes. The Department of Energy

will provide public access to these results of federally sponsored research in accordance with the DOE Public Access Plan(<http://energy.gov/downloads/doepublic-access-plan>).

-
- [1] V. M. Goldschmidt, *Naturwissenschaften* **14**, 477 (1926).
- [2] M. W. Lufaso and P. M. Woodward, *Acta Crystallographica Section B* **57**, 725 (2001).
- [3] M. W. Lufaso, P. W. Barnes, and P. M. Woodward, *Acta Crystallographica Section B* **62**, 397 (2006).
- [4] D. M. Giaquinta and H.-C. zur Loye, *Chemistry of Materials* **6**, 365 (1994).
- [5] N. Das, S. Singh, A. G. Joshi, M. Thirumal, V. R. Reddy, L. C. Gupta, and A. K. Ganguli, *Inorganic Chemistry* **56**, 12712 (2017).
- [6] M. J. Davis, S. J. Mugavero III, K. I. Glab, M. D. Smith, and H.-C. zur Loye, *Solid State Sciences* **6**, 413 (2004).
- [7] H. L. Feng, M. Arai, Y. Matsushita, Y. Tsujimoto, Y. Guo, C. I. Sathish, X. Wang, Y.-H. Yuan, M. Tanaka, and K. Yamaura, *Journal of the American Chemical Society* **136**, 3326 (2014).
- [8] T. Ferreira, G. Morrison, J. Yeon, and H.-C. zur Loye, *Crystal Growth & Design* **16**, 2795 (2016).
- [9] W. R. Gemmill, M. D. Smith, R. Prozorov, and H.-C. zur Loye, *Inorganic Chemistry* **44**, 2639 (2005).
- [10] P. Kayser, J. A. Alonso, A. Muñoz, and M. T. Fernández-Díaz, *Acta Materialia* **126**, 114 (2017).
- [11] G. King, S. Thimmaiah, A. Dwivedi, and P. M. Woodward, *Chemistry of Materials* **19**, 6451 (2007).
- [12] G. King, A. S. Wills, and P. M. Woodward, *Phys. Rev. B* **79**, 224428 (2009).
- [13] M.-R. Li, J. P. Hodges, M. Retuerto, Z. Deng, P. W. Stephens, M. C. Croft, X. Deng, G. Kotliar, J. Sánchez-Benítez, D. Walker, and M. Greenblatt, *Chemistry of Materials* **28**, 3148 (2016).
- [14] R. Macquart, S.-J. Kim, W. R. Gemmill, J. K. Stalick, Y. Lee, T. Vogt, and H.-C. zur Loye, *Inorganic Chemistry* **44**, 9676 (2005).
- [15] R. Morrow, R. Mishra, O. D. Restrepo, M. R. Ball, W. Windl, S. Wurmehl, U. Stockert, B. Büchner, and P. M. Woodward, *Journal of the American Chemical Society* **135**, 18824 (2013).
- [16] R. Morrow, J. Yan, M. A. McGuire, J. W. Freeland, D. Haskel, and P. M. Woodward, *Phys. Rev. B* **92**, 094435 (2015).
- [17] R. Morrow, K. Samanta, T. Saha Dasgupta, J. Xiong, J. W. Freeland, D. Haskel, and P. M. Woodward, *Chemistry of Materials* **28**, 3666 (2016).
- [18] S. J. Mugavero III, A. H. Fox, M. D. Smith, and H.-C. zur Loye, *Journal of Solid State Chemistry* **183**, 465 (2010).
- [19] H. L. Feng, Z. Deng, M. Wu, M. Croft, S. H. Lapidus, S. Liu, T. A. Tyson, B. D. Ravel, N. F. Quackenbush, C. E. Frank, C. Jin, M.-R. Li, D. Walker, and M. Greenblatt, *Inorganic Chemistry* **58**, 397 (2019).
- [20] H. L. Feng, M. Reehuis, P. Adler, Z. Hu, M. Nicklas, A. Hoser, S.-C. Weng, C. Felser, and M. Jansen, *Phys. Rev. B* **97**, 184407 (2018).
- [21] H. L. Feng, S. Calder, M. P. Ghimire, Y.-H. Yuan, Y. Shirako, Y. Tsujimoto, Y. Matsushita, Z. Hu, C.-Y. Kuo, L. H. Tjeng, T.-W. Pi, Y.-L. Soo, J. He, M. Tanaka, Y. Katsuya, M. Richter, and K. Yamaura, *Phys. Rev. B* **94**, 235158 (2016).
- [22] Y. Yuan, H. L. Feng, M. P. Ghimire, Y. Matsushita, Y. Tsujimoto, J. He, M. Tanaka, Y. Katsuya, and K. Yamaura, *Inorganic Chemistry* **54**, 3422 (2015).
- [23] P. Kayser, J. A. Alonso, F. J. Mompeán, M. Retuerto, M. Croft, A. Ignatov, and M. T. Fernández-Díaz, *European Journal of Inorganic Chemistry* **2015**, 5027 (2015).
- [24] H. L. Feng, P. Adler, M. Reehuis, W. Schnelle, P. Pattison, A. Hoser, C. Felser, and M. Jansen, *Chemistry of Materials* **29**, 886 (2017).
- [25] J. Park, E. Vescovo, H. Kim, C. Kwon, R. Ramesh, and T. Venkatesan, *Nature* **392**, 794 (1998).
- [26] R. Cohen, *Nature* **358**, 136 (1992).
- [27] S. Calder, V. O. Garlea, D. F. McMorrow, M. D. Lumsden, M. B. Stone, J. C. Lang, J.-W. Kim, J. A. Schlueter, Y. G. Shi, K. Yamaura, Y. S. Sun, Y. Tsujimoto, and A. D. Christianson, *Phys. Rev. Lett.* **108**, 257209 (2012).
- [28] D. Pesin and L. Balents, *Nature Phys.* **6**, 376 (2010).
- [29] Y. K. Kim, N. H. Sung, J. D. Denlinger, and B. J. Kim, *Nature Physics* **12**, 37 (2016).
- [30] B. J. Kim, H. Ohsumi, T. Komesu, S. Sakai, T. Morita, H. Takagi, and T. Arima, *Science* **323**, 1329 (2009).
- [31] S. Calder, J. G. Vale, N. A. Bogdanov, X. Liu, C. Donnerer, M. H. Upton, D. Casa, A. H. Said, M. D. Lumsden, Z. Zhao, J. Q. Yan, D. Mandrus, S. Nishimoto, J. van den Brink, J. P. Hill, D. F. McMorrow, and A. D. Christianson, *Nature Communications* **7**, 11651 (2016).
- [32] G. Cao, A. Subedi, S. Calder, J.-Q. Yan, J. Yi, Z. Gai, L. Poudel, D. J. Singh, M. D. Lumsden, A. D. Christianson, B. C. Sales, and D. Mandrus, *Phys. Rev. B* **87**, 155136 (2013).
- [33] I. V. Solov'ev, V. V. Mazurenko, and A. A. Katanin, *Phys. Rev. B* **92**, 235109 (2015).
- [34] M. A. Laguna-Marco, P. Kayser, J. A. Alonso, M. J. Martínez-Lope, M. van Veenendaal, Y. Choi, and D. Haskel, *Phys. Rev. B* **91**, 214433 (2015).
- [35] S. H. Chun, J. W. Kim, J. Kim, H. Zheng, C. C. Stoumpos, C. D. Malliakas, J. F. Mitchell, K. Mehlawat, Y. Singh, Y. Choi, T. Gog, A. Al-Zein, M. M. Sala, M. Krisch, J. Chaloupka, G. Jackeli, G. Khaliullin, and B. J. Kim, *Nature Phys.* **11**, 462 (2015).
- [36] S. Bhowal, S. Baidya, I. Dasgupta, and T. Saha-Dasgupta, *Phys. Rev. B* **92**, 121113 (2015).
- [37] H. Watanabe, T. Shirakawa, and S. Yunoki, *Phys. Rev. Lett.* **110**, 027002 (2013).
- [38] Y. Singh, S. Manni, J. Reuther, T. Berlijn, R. Thomale, W. Ku, S. Trebst, and P. Gegenwart, *Phys. Rev. Lett.* **108**, 127203 (2012).
- [39] D. Haskel, G. Fabbris, M. Zhernenkov, P. P. Kong, C. Q. Jin, G. Cao, and M. van Veenendaal, *Phys. Rev. Lett.* **109**, 027204 (2012).
- [40] G. Jackeli and G. Khaliullin, *Phys. Rev. Lett.* **102**, 017205 (2009).
- [41] H. Müller-Buschbaum, *Zeitschrift für anorganische und allgemeine Chemie* **635**, 1065 (2009).
- [42] R. Morrow, J. R. Soliz, A. J. Hauser, J. C. Gallagher, M. A. Susner, M. D. Sumption, A. A. Aczel, J. Yan, F. Yang, and P. M. Woodward, *Journal of Solid State Chemistry* **238**, 46 (2016).

- [43] J. Kanamori, *Journal of Physics and Chemistry of Solids* **10**, 87 (1959).
- [44] A. K. Paul, M. Reehuis, V. Ksenofontov, B. Yan, A. Hoser, D. M. Többs, P. M. Abdala, P. Adler, M. Jansen, and C. Felser, *Phys. Rev. Lett.* **111**, 167205 (2013).
- [45] A. E. Taylor, R. Morrow, M. D. Lumsden, S. Calder, M. H. Upton, A. I. Kolesnikov, M. B. Stone, R. S. Fishman, A. Paramakanti, P. M. Woodward, and A. D. Christianson, *Phys. Rev. B* **98**, 214422 (2018).
- [46] V. O. Garlea, B. C. Chakoumakos, S. A. Moore, G. B. Taylor, T. Chae, R. G. Maples, R. A. Riedel, G. W. Lynn, and D. L. Selby, *Applied Physics A* **99**, 531 (2010).
- [47] S. Calder, K. An, R. Boehler, C. R. Dela Cruz, M. D. Frontzek, M. Guthrie, B. Haberl, A. Huq, S. A. J. Kimber, J. Liu, J. J. Molaison, J. Neufeind, K. Page, A. M. dos Santos, K. M. Taddei, C. Tulk, and M. G. Tucker, *Review of Scientific Instruments* **89**, 092701 (2018).
- [48] J. Rodríguez-Carvajal, *Physica B: Condensed Matter* **192**, 55 (1993).
- [49] J. Perez-Mato, S. Gallego, E. Tasci, L. Elcoro, G. de la Flor, and M. Aroyo, *Annual Review of Materials Research* **45**, 217 (2015).
- [50] Aroyo, M. I., Perez-Mato, J. M., Orobengoa, D., Tasci, E., G. de la Flor, and A. Kirov, *Bulgarian Chemical Communications* **43**, 183 (2011).
- [51] A. Wills, *Physica B* **276**, 680 (2000).
- [52] See Supplemental Material.
- [53] Y. Shvyd'ko, J. Hill, C. Burns, D. Coburn, B. Brajuskovic, D. Casa, K. Goetze, T. Gog, R. Khachatryan, J.-H. Kim, C. Kodituwakku, M. Ramanathan, T. Roberts, A. Said, H. Sinn, D. Shu, S. Stoupin, M. Upton, M. Wiczorek, and H. Yavas, *Journal of Electron Spectroscopy and Related Phenomena* **188**, 140 (2013), progress in Resonant Inelastic X-Ray Scattering.
- [54] P. Blaha, K. Schwarz, G. Madsen, D. Kvasnicka, and J. Luitz, *WIEN2k, An Augmented Plane Wave + Local Orbitals Program for Calculating Crystal Properties* (K. Schwarz, Tech. Univ. Wien, Austria, 2001).
- [55] J. P. Perdew, K. Burke, and M. Ernzerhof, *Phys. Rev. Lett.* **77**, 3865 (1996).
- [56] M. Rezaigui, W. Benstaali, A. Abbad, S. Bentata, and B. Bouhafs, *Journal of Superconductivity and Novel Magnetism* **30**, 2581 (2017).
- [57] A. A. Aczel, J. P. Clancy, Q. Chen, H. D. Zhou, D. Reig-i Plessis, G. J. MacDougall, J. P. C. Ruff, M. H. Upton, Z. Islam, T. J. Williams, S. Calder, and J.-Q. Yan, *Phys. Rev. B* **99**, 134417 (2019).
- [58] A. Revelli, C. C. Loo, D. Kiese, P. Becker, T. Fröhlich, T. Lorenz, M. Moretti Sala, G. Monaco, F. L. Buessen, J. Attig, M. Hermanns, S. V. Streltsov, D. I. Khomskii, J. van den Brink, M. Braden, P. H. M. van Loosdrecht, S. Trebst, A. Paramakanti, and M. Grüninger, *Phys. Rev. B* **100**, 085139 (2019).
- [59] J. Song, B. Zhao, L. Yin, Y. Qin, J. Zhou, D. Wang, W. Song, and Y. Sun, *Dalton Trans.* **46**, 11691 (2017).
- [60] N. Sirica, P. Vilmercati, F. Bondino, I. Pis, S. Nappini, S. K. Mo, A. V. Fedorov, P. K. Das, I. Vobornik, L. L. J. Fujii, D. Sapkota, D. S. Parker, D. G. Mandrus, and N. Mannella, *Nature Mat* **12**, 707 (2013).
- [61] T. N. Lamichhane, V. Taufour, M. W. Masters, D. S. Parker, U. S. Kaluarachchi, S. Thimmaiah, S. L. Bud'ko, and P. C. Canfield, *Applied Physics Letters* **109**, 092402 (2016).
- [62] T. Pandey, M.-H. Du, and D. S. Parker, *Phys. Rev. Applied* **9**, 034002 (2018).